

$$t_m(z) = -\frac{H}{\lambda_H - \dot{m}} \ln \left(\frac{1 - \frac{\dot{m}}{\lambda_H} z + \frac{\dot{m}}{\lambda_H}}{H} \right)$$

where t_m is the model age of ice at a depth $d = (H - z)$.

22. If the melt rate exceeds the surface accumulation rate, the thickness of an annual layer actually increases with age and depth in the ice (which is equivalent to saying that there is net convergence of flow in the horizontal plane or a slow-down along flow in a flow-line model). This situation occurs in several areas in northeast Greenland. The thinning rate can be expressed with a thinning rate factor

$$f = \frac{\dot{\epsilon}_{D-J}}{\dot{\epsilon}_{Nye}}, h > 0; f = \frac{\dot{\epsilon}_{melt}}{\dot{\epsilon}_{Nye}} = 1 - \frac{\dot{m}}{\lambda_H}, h = 0$$

which is the ratio of the strain rate required by the best-fit age-depth relation divided by the Nye strain rate. It is greater than 1 for a Dansgaard-Johnsen fit, and less than 1 for a Nye-with-melting fit.

23. The details of this fit are covered in Fahnestock and others (15). The misfit function is

$$f(\lambda_H, h) = \sum_{i=1}^n \left[\frac{t_m(\lambda_H, h, d(i)) - t(i)}{t(i)} \right]^2$$

24. D. Dahl-Jensen, S. J. Johnsen, C. U. Hammer, H. B. Clausen, J. Jouzel, in *Ice in the Climate System*, W. R. Peltier, Ed. (Springer-Verlag, Berlin, 1993), vol. 1(12), pp. 517–532.
25. K. M. Cuffey, G. D. Clow, *J. Geophys. Res.* **102**, 26383 (1997).
26. The misfit function for the Nye model modified to allow melting is

$$f(\lambda_H, \dot{m}) = \sum_{i=1}^n \left[\frac{t_m(\lambda_H, \dot{m}, d(i)) - t(i)}{t(i)} \right]^2$$

The modified Nye model returned a more smoothly varying estimate of accumulation rate along the flight in the areas where the Dansgaard-Johnsen model returned $h < 0$.

27. The spatial variations in accumulation patterns compare well with patterns determined from shallow firn cores and snow pits by the NASA PARCA program and earlier work.
28. I. R. Joughin, M. A. Fahnestock, J. L. Bamber, *Ann. Glaciol.* **31**, 141 (2000).
29. M. A. Fahnestock et al., *J. Geophys. Res.*, in press.
30. W. S. B. Paterson, *The Physics of Glaciers* (Elsevier Science Ltd., Oxford, ed. 3, 1994), pp. 215–235 and 318–354.
31. J. G. Sclater, C. Jaupart, D. Galson, *Rev. Geophys.* **18**, 269 (1980).
32. J. M. Brozena, thesis, University of Cambridge (1996).
33. ———, *The Greenland Aerogeophysics Project: Airborne Gravity, Topographic and Magnetic Mapping of an Entire Continent*, IAG Symposium No. 110, 20 August 1991, Vienna, Austria (Springer-Verlag, New York, 1991), pp. 203–214.
34. J. Brozena, M. Chalonga, R. Forsberg, G. Mader, *Eos* **74**, 18 (1993).
35. R. B. Smith, L. W. Braille, *J. Volcanol. Geotherm. Res.* **61**, 121 (1994).
36. Modeled results from the GISP2 core suggest that the accumulation rate has only been slowly increasing over the last 9000 years. This result, barring a change in average storm tracks, may well be applicable to other parts of the inland ice. The assumption that the ice thickness has been constant over this interval is perhaps less well supported by the available data. A rapid increase in ice thickness (at approximately half the accumulation rate) would produce an age-depth relation in the upper (younger) layers that showed slower than expected thinning rates. This would translate into an estimate that included basal melting using our technique. However, this would predict a basal melt rate that was essentially the same as the thickening rate. The basal melting we identify is larger than any measured thickening, and the spatial patterns of melting and thickening do not match.

37. C. H. Davis, C. A. Kluever, B. J. Haines, *Science* **279**, 2086 (1998).
38. H. J. Zwally, M. B. Giovinetto, *Ann. Glaciol.* **31**, 126 (2000).
39. T. A. Scambos, M. A. Fahnestock, *J. Glaciol.* **44**, 97 (1998).
40. Supported by NASA Headquarters Program for Arctic

Regional Climate Assessment (PARCA) (M.F., W.A., I.J., and P.G.). Analysis of the airborne gravity and magnetic data (J.B.) were supported under Program Element 61153N of the ONR 6.1 program. We thank C. Shuman, T. Scambos, and two anonymous reviewers for reviewing the manuscript.

14 August 2001; accepted 25 October 2001

A New Global Mode of Earth Deformation: Seasonal Cycle Detected

Geoffrey Blewitt,^{1,2*} David Lavallée,¹ Peter Clarke,² Konstantin Nurutdinov²

We have detected a global mode of Earth deformation that is predicted by theory. Precise positioning of Global Positioning System sites distributed worldwide reveals that during February to March, the Northern Hemisphere compresses (and the Southern Hemisphere expands), such that sites near the North Pole move downward by 3.0 millimeters, and sites near the equator are pulled northward by 1.5 millimeters. The opposite pattern of deformation occurs during August to September. We identify this pattern as the degree-one spherical harmonic response of an elastic Earth to increased winter loading of soil moisture, snow cover, and atmosphere. Data inversion shows the load moment's trajectory as a great circle traversing the continents, peaking at 6.9×10^{22} kilogram meters near the North Pole in winter, indicating interhemispheric mass exchange of $1.0 \times 10^{16} \pm 0.2 \times 10^{16}$ kilograms.

Redistribution of mass over Earth's surface generates changes in gravitational and surface forces that produce a stress response in the solid Earth, accompanied by characteristic patterns of surface deformation (1–3). Here, we search for global deformation resulting from Earth's elastic response to a change in the “load moment” (a dipole moment), defined as the load center of mass vector multiplied by the load mass. This predicted degree-one spherical harmonic mode (1, 4) has unique characteristics that distinguish it from tidal deformation. Our calculations predict that the known seasonal exchange of water and air between the Northern and Southern hemispheres (5–7) is of sufficient magnitude to force such a mode with annual period at the several-millimeter level, which ought to be detectable by modern geodetic techniques. Monitoring this mode should enable global characterization of the hydrological cycle through direct inversion of geodetic data, and enable determination of mechanical properties of Earth on the global scale.

Previous investigations in space-based geodesy have detected displacements of surface

height at the 10-mm level in response to variation in atmospheric pressure (8) and large-scale terrestrial water storage (9). Such results show statistically significant correlation between observed site position variations and model predictions. Although promising, the residual discrepancies between data and models remain at least as large as the predicted signal. Apart from current uncertainties in modeling groundwater storage, another limitation is the level of noise in globally referenced site position data (9). We mitigate these problems by seeking a deformation mode with a theoretical functional form (allowing for inversion) and large-scale spatio-temporal coherence (enhancing the signal-to-noise ratio).

The change in Earth's shape due to the gravitational and pressure stresses of surface loading is theoretically characterized by spherical harmonic potential perturbations and load Love numbers (2). Load Love number theory is fundamental to the Green's function approach to loading models (1), which has facilitated numerical computation of Earth deformation due to arbitrary load distributions (3). Unlike tidal theory, loading theory includes a degree-one deformation generated by movement of the load center of mass with respect to the solid Earth center of mass (1, 4, 10).

Let us define CM as the center of mass of the solid Earth plus the load, and CE as the center of mass of the solid Earth only. CM

¹Nevada Bureau of Mines and Geology, and Seismological Laboratory, University of Nevada, Reno, NV 89557, USA. ²Department of Geomatics, University of Newcastle, Newcastle upon Tyne, NE1 7RU, UK.

*To whom correspondence should be addressed. E-mail: gblewitt@unr.edu

REPORTS

moves undisturbed in inertial space as the load is redistributed. Conservation of linear momentum requires that redistribution of surface mass displaces CE with respect to CM by the amount (4)

$$\Delta \mathbf{r}_{\text{CE}} = -M_L \Delta \mathbf{r}_L / M_{\oplus} = -\mathbf{m} / M_{\oplus} \quad (1)$$

where $M_{\oplus} = 6.0 \times 10^{24}$ kg is Earth system's mass, M_L is net mass of load that has been transported over Earth's surface, and $\Delta \mathbf{r}_L$ is the change in center of mass of the transported load in the CE frame. We define the "load moment" vector $\mathbf{m} = M_L \Delta \mathbf{r}_L$ to emphasize the characteristic of the load that forces this mode of deformation (and to which the data are sensitive). To the first order, the displacement of CE creates a tide-raising potential $V_1(\phi, \lambda)$ in the CE frame at latitude ϕ and longitude λ

$$V_1(\phi, \lambda) = -g \hat{\mathbf{h}} \cdot \Delta \mathbf{r}_{\text{CE}} = g \hat{\mathbf{h}} \cdot \mathbf{m} / M_{\oplus} \quad (2)$$

where $\hat{\mathbf{h}}(\phi, \lambda)$ is the unit vector pointing locally upward, and g is acceleration due to gravity. Equation 2 is a pure degree-one spherical harmonic function, to which load Love number theory is directly applicable. We assume it is reasonable to ignore the higher degree harmonics, because they are orthogonal to the degree-one harmonics and would not significantly bias the results for a well-distributed global network (11). Solutions for surface displacements in the CE frame have been derived in complex spherical harmonic form (4); however, we have derived solutions in concise vector form

$$\begin{aligned} \Delta \bar{s}_h &= h'_1 V_1 / g = h'_1 \hat{\mathbf{h}} \cdot \mathbf{m} / M_{\oplus} \\ \Delta \bar{s}_l &= l'_1 \hat{\mathbf{l}} \cdot \nabla V_1 / g = l'_1 \hat{\mathbf{l}} \cdot \mathbf{m} / M_{\oplus} \end{aligned} \quad (3)$$

where $\Delta \bar{s}_h$ is upward displacement, $\Delta \bar{s}_l$ is displacement in any lateral direction $\hat{\mathbf{l}}$, and surface gradient operator $\nabla = \hat{\phi} \partial_{\phi} + \hat{\lambda} (1/\cos \phi) \partial_{\lambda}$. We use load Love numbers modeled by Farrell (1), $h'_1 = -0.290$ and $l'_1 = 0.113$, which are specified in the CE frame.

This global mode of deformation is unique, in that it compresses the hemisphere centered on the load moment, and expands the opposite hemisphere, such that a perfect sphere deforms to another perfect (but strained) sphere of identical diameter. The surface everywhere stretches laterally toward the pole of the load moment. We discovered that this mode has the peculiar property that there exist reference frames in which the surface deformation field is either purely vertical or purely horizontal. Such an extreme range of equivalent kinematics underscores the need for reference frame consistency when comparing data with models.

Here, we use the center of figure frame (CF), defined as having no-net translation with respect to the three-dimensional surface displacement field. This is an appropriate frame to describe deformations, because only relative surface displacement data contribute to the solution; the CE frame is not directly observable, and the CM frame accuracy is limited by model

errors in nongravitational satellite accelerations (12). Transformation to the CF frame is accomplished by subtracting from the displacement field the average displacement $\Delta \mathbf{r}_{\text{CF}}$ in the CE frame (4), which is derived by surface integration of Eq. 3

$$\Delta \mathbf{r}_{\text{CF}} = \frac{1}{3} (h'_1 + 2l'_1) \mathbf{m} / M_{\oplus} \quad (4)$$

where $\Delta \mathbf{r}_{\text{CF}}$ is CF variation in the CE frame. The vector form of Eq. 3 readily allows us to express displacements in the CF frame

$$\Delta \bar{s}_h = \Delta \bar{s}_h - \hat{\mathbf{h}} \cdot \Delta \mathbf{r}_{\text{CF}} = -\frac{2}{3} (l'_1 - h'_1) \hat{\mathbf{h}} \cdot \mathbf{m} / M_{\oplus} \quad (5)$$

$$\Delta \bar{s}_l = \Delta \bar{s}_l - \hat{\mathbf{l}} \cdot \Delta \mathbf{r}_{\text{CF}} = +\frac{1}{3} (l'_1 - h'_1) \hat{\mathbf{l}} \cdot \mathbf{m} / M_{\oplus}$$

Thus, by analogy with Eq. 2, Farrell's load Love numbers in the CF frame are $l'_1 = \frac{1}{3} (l'_1 - h'_1) = 0.134$ and $\bar{h}'_1 = -2l'_1 = -0.268$. Hence, we can express site displacements in the CF frame $\Delta \bar{\mathbf{s}} = (\Delta \bar{s}_x, \Delta \bar{s}_y, \Delta \bar{s}_z)^T$ by the matrix equation

$$\Delta \bar{\mathbf{s}} = l'_1 \mathbf{G}^T \text{diag}[+1, +1, -2] \mathbf{G} \mathbf{m} / M_{\oplus} \quad (6)$$

where \mathbf{G} is the 3×3 matrix that rotates geocentric into topocentric displacements (east, north, and up). Through measurement of site displacements globally, we can invert Eq. 6 to solve for the components of load moment $\mathbf{m} = (m_x, m_y, m_z)^T$. Alternatively, if the load variation is assumed or known from some independent data source or model, then inverting Eq. 6 for the degree-one load Love number can test Earth's mechanical properties.

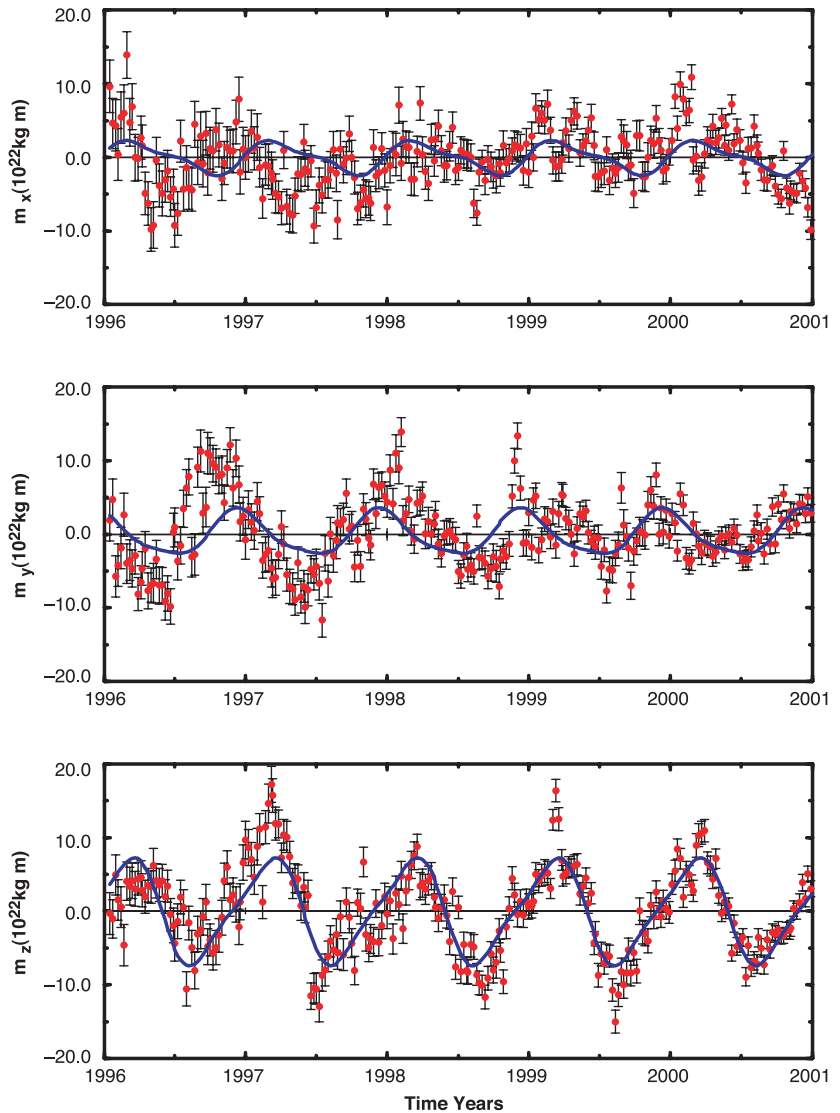


Fig. 1. Estimates of load moment components. Weekly estimates (red) are for (A) x direction toward the intersection of the Greenwich meridian and the equator, (B) y direction, and (C) z direction toward the North Pole. Superimposed is the empirical model (blue) given by Table 1. The weighted root mean square of the time series before/after subtracting the empirical model are (in 10^{22} kg m) 3.9/3.7, 4.2/3.4, and 5.5/2.9, corresponding to square root variance reductions of 1.2, 2.5, and 4.7.

REPORTS

We applied this theory to 5 years of Global Positioning System (GPS) data, acquired by 66 stations of the International GPS Service (IGS) network (13). Every week at Newcastle's IGS Global Network Associate Analysis Center, free-network solutions in the CM frame were analyzed to produce site coordinate time series in the CF frame (14). The time series were de-trended to remove plate tectonic motion, accounting for correlations between velocity and annual signals (15). The resulting time series have a root mean square of ~ 3 mm

(horizontal) and ~ 7 mm (vertical). Equation 6 was inverted by weighted least-squares to solve for the load moment every week.

The load moment results (Fig. 1) show annual oscillations, especially in the z (polar) direction, corresponding to net seasonal mass transport between the Northern and Southern hemispheres. The maximum downward deformation (Fig. 2) of 3.0 mm points close to the North Pole during February to March, and the South Pole during August to September. Corresponding lateral deformation of 1.5 mm is

Fig. 2. Observed seasonal variation in Earth deformation. The degree-one surface deformation field uses two-month stacked solutions for (top to bottom) December-January, February-March, April-May, June-July, August-September, and October-November. The left panel refers to vertical deformation, and the right panel to the magnitude of horizontal deformation. Horizontal displacements always point toward the location of maximum downward displacement.

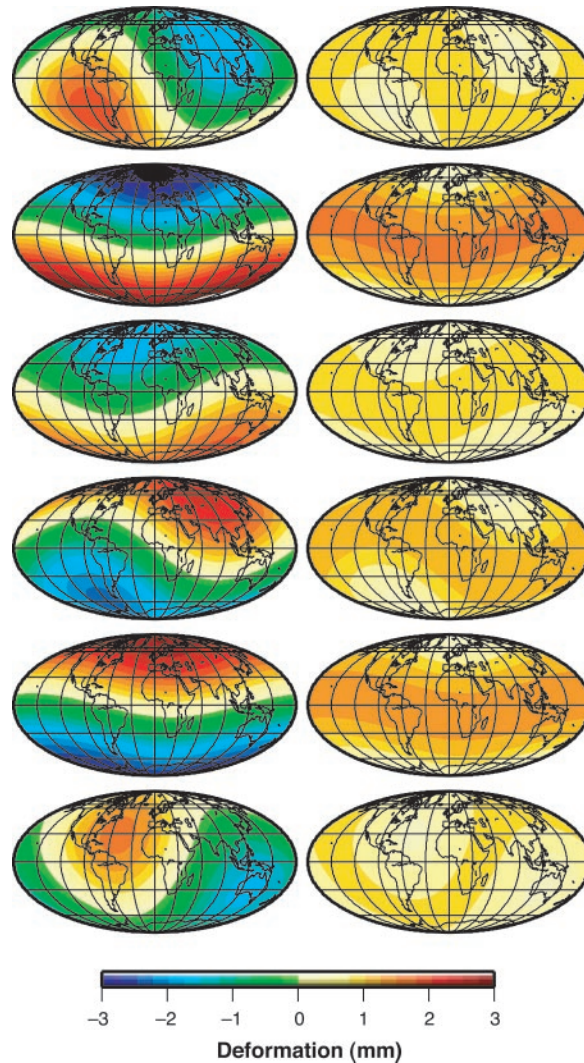


Table 1. Empirical seasonal load moment model. Amplitude and phases are defined by $A_i \cos[2\pi f_i(t - t_0) - \Phi_i]$ where t_0 is 1 January and f_i is frequency. All parameter values were derived by weighted least squares using the load moment time series (Fig. 1). The 1-standard deviation uncertainties are propagated from scaled coordinate errors (14), but do not account for inadequacies of the empirical model, for example, due to interannual variability.

Load moment component	Annual amplitude A_1 (10^{22} kg m)	Annual phase Φ_1 (degrees)	Semiannual amplitude A_2 (10^{22} kg m)	Semiannual phase Φ_2 (degrees)
m_x	2.0 ± 0.2	86 ± 3	0.7 ± 0.2	69 ± 13
m_y	2.9 ± 0.2	345 ± 3	0.6 ± 0.2	301 ± 13
m_z	6.6 ± 0.1	56 ± 1	1.5 ± 0.1	207 ± 5

observed near the equator at these times. The load moment migrates through the year, following the approximate surface trajectory of a great circle (Fig. 3). The maximum load moment is 6.9×10^{22} kg m in the period from February to March. The minimum load is observed when it rapidly crosses the equator southward during May over South America, and northward during November over Indonesia. We used our load moment time series to produce an empirical seasonal model, estimating amplitudes and phases of annual and semiannual load moment variations (Table 1 and Figs. 1 and 3). The annual z component of the load moment peaks at 6.6×10^{22} kg m toward the ends of February and August. The empirical seasonal model and Eq. 6 form a predictive calibration model to reduce annual signals in geodetic data (15), say, for plate tectonics (although more regional effects may dominate individual site time series). The statistics from fitting the time series (Fig. 1) indicate that the precision of our weekly load moment estimates is 3.6×10^{22} kg m (1 standard deviation).

Our results provide constraints on models of mass redistribution. Taking extreme examples, a load moment of 6.6×10^{22} kg m would be produced by net transport of (i) 0.5×10^{16} kg from the South Pole to the

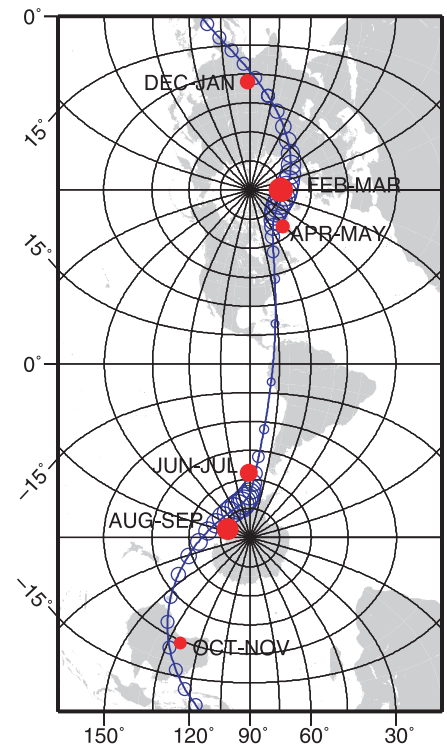


Fig. 3. Trajectory of the load moment as it travels through the year. Each load moment (solid red) is the two-monthly weighted average of the weekly load moments, stacked over 5 years. The radius of each symbol is proportional to the magnitude. The maximum load moment is 6.9×10^{22} kg m in February-March. The empirical seasonal model (open circles; see Table 1) is also plotted for each week.

North Pole; (ii) 1.4×10^{16} kg uniformly distributed from one hemisphere to the other; or (iii) 1.1×10^{16} kg from the oceans to land at high latitudes. We suggest that any reasonable model should therefore have a total seasonal transported mass within 40% of 1.0×10^{16} kg. Secondly, models should predict that the load peaks near the poles in their respective late-winter seasons. Thirdly, models should predict that the load's trajectory follows an approximate great circle over the continents (Fig. 3).

From remote sensing, it is known that the mass of snow in the Northern Hemisphere peaks during February to March at 0.3×10^{16} kg (5, 16). Recent analysis in atmospheric research (6) confirms earlier interpretations (7) on the existence of interhemispheric oscillations in atmospheric mass at the level of 0.4×10^{16} kg, which appears to be driven in part by anomalous cooling over snow-covered areas, particularly over Siberia and Canada (17). Our results therefore suggest that the observed pattern of deformation is dominated by winter groundwater storage enhanced by atmospheric pressure. Assuming an upper bound on the net redistributed mass at 1.4×10^{16} kg, we infer the non-snow component of winter groundwater to be $<0.7 \times 10^{16}$ kg.

The load's trajectory over the continents (in approximately the y - z plane) is consistent with the land's ability to sustain loads (unlike the ocean's tendency to rapidly approach equilibrium). An interesting feature of the load moment time series is the asymmetric pattern of z oscillations (Fig. 1) and the rapid southward equatorial crossing of mass (Fig. 3) in May. This is consistent with rapid water runoff, which is known to peak during late spring in the Northern Hemisphere (18). A small y component of load moment also appears during the transition seasons traversing regions of known intense hydrological loading (9) in southeast Asia and South America (Fig. 2). An anomaly in the $\pm y$ direction is apparent during 1996/1997, immediately preceding the 1997/1998 El Niño event. Possible mechanisms that might enhance the y component include an equatorial oscillation in (nonsteric) sea level across the Pacific (driven by wind stress) and anomalous monsoon precipitation over land.

To conclude, we detected a global-scale mode of Earth deformation that we have identified as the response of an elastic Earth to redistribution of surface load, specifically the degree-one spherical harmonic mode that theoretically corresponds to change in the load moment. This mode compresses one hemisphere and expands the opposite hemisphere in such a manner that it does not change Earth's overall shape, but nevertheless stretches its surface and so affects site coordinates. In Earth's center-of-figure frame, the poles appear to be displaced downward by 3.0 mm during their respective win-

ters, and the equator appears to move toward the winter pole by 1.5 mm. Our inversion procedure produces a load moment time series with an annual signal in Earth's polar direction with amplitude 6.6×10^{22} kg m. Stacking reveals that the load moment follows the approximate trajectory of a great circle traversing the continents, peaking at 6.9×10^{22} kg m near the North Pole in winter. These results are consistent with seasonal loading of land surfaces by fluids, corresponding to an annual mass exchange of $1.0 \pm 0.2 \times 10^{16}$ kg between the hemispheres.

References and Notes

1. W. E. Farrell, *Rev. Geophys. Space Phys.* **10**, 761 (1972).
2. E. W. Grafarend, J. Engels, P. Varga, *J. Geodesy* **72**, 11 (1997).
3. T. van Dam, J. M. Wahr, *Phys. Chem. Earth* **23**, 1077 (1998).
4. A. S. Trupin, M. F. Meier, J. M. Wahr, *Geophys. J. Int.* **108**, 1 (1992).
5. B. F. Chao, W. P. O'Connor, A. T. C. Chang, D. K. Hall, J. L. Foster, *J. Geophys. Res.* **92**, 9415 (1987).
6. Z. Guan, T. Yamagata, *Geophys. Res. Lett.* **28**, 263 (2001).
7. K. Trenberth, *J. Geophys. Res.* **86**, 5238 (1981).
8. T. van Dam, G. Blewitt, M. B. Hefflin, *J. Geophys. Res.* **99**, 23939 (1994).

9. T. van Dam *et al.*, *Geophys. Res. Lett.* **28**, 651 (2001).
10. M. Greff-Lefftz, H. Legros, *Geophys. J. Int.* **131**, 699 (1997).
11. For deformations up to degree n , a network can be considered "well distributed" if neighboring stations everywhere are spaced much less than $180^\circ/n$, which for $n = 1$ implies multiple stations in arbitrary hemispheres.
12. J. L. Chen, C. R. Wilson, R. J. Eanes, R. S. Nerem, *J. Geophys. Res.* **104**, 2683 (1999).
13. Information on relevant GPS station data is provided at www.sciencemag.org/cgi/content/full/294/5550/2342/DC1.
14. P. Davies, G. Blewitt, *J. Geophys. Res.* **105**, 11083 (2000).
15. G. Blewitt, D. Lavallée, *J. Geophys. Res.*, in press.
16. A. T. C. Chang, J. L. Foster, D. K. Hall, *Remote Sens. Lett. Int. J. Remote Sens.* **11**, 167 (1990).
17. J. Cohen, K. Saito, D. Entekhabi, *Geophys. Res. Lett.* **28**, 299 (2001).
18. B. M. Fekete, C. J. Vörösmarty, W. Grabs, *WMO-Global Runoff Data Centre Report 22* (Koblenz, Germany, 1999).
19. We thank J. Wahr and V. Dehant for comments, and IGS for providing data. Supported by U.S. Department of Energy grant DE-FC08-98NV12081, NASA grant SENH99-0325-0015, U.K. Natural Environment Research Council grant GR3/11976, and a University of Nevada Reno international activities grant. We thank NSF for supporting continuation of this research.

13 August 2001; accepted 7 November 2001

A High-Resolution Absolute-Dated Late Pleistocene Monsoon Record from Hulu Cave, China

Y. J. Wang,^{1,3} H. Cheng,² R. L. Edwards,^{2*} Z. S. An,³ J. Y. Wu,⁴ C.-C. Shen,⁵ J. A. Dorale⁶

Oxygen isotope records of five stalagmites from Hulu Cave near Nanjing bear a remarkable resemblance to oxygen isotope records from Greenland ice cores, suggesting that East Asian Monsoon intensity changed in concert with Greenland temperature between 11,000 and 75,000 years before the present (yr. B.P.). Between 11,000 and 30,000 yr. B.P., the timing of changes in the monsoon, as established with ²³⁰Th dates, generally agrees with the timing of temperature changes from the Greenland Ice Sheet Project Two (GISP2) core, which supports GISP2's chronology in this interval. Our record links North Atlantic climate with the meridional transport of heat and moisture from the warmest part of the ocean where the summer East Asian Monsoon originates.

The Asian and Australian Monsoons are important because they transport heat and moisture from the warmest part of the tropical ocean (the West Pacific Warm Pool) across the equator and to higher latitudes. The East Asian Monsoon, a sub-system of the Asian Monsoon, affects an area east of the Bay of Bengal and the Tibetan Plateau (1). Spring heating of Asia initiates the summer monsoon, which transports northward moisture and heat from north of Australia across the Warm Pool, as far as northern China. The winter monsoon is characterized by cold, dry

Siberian air flowing southward across eastern China, ultimately contributing to the Australian summer monsoon (1).

Plausible factors affecting the monsoon are orbitally controlled changes in insolation (2, 3), shifts in sea level causing changes in Warm Pool surface area (4), and circulation changes internal to the climate system (5). Loess records (6, 7) show clear evidence for monsoon changes (1) that are possibly linked to global climate (7) and Heinrich Events (5). However, resolution and dating problems limit the loess work. We reconstruct mon-

A New Global Mode of Earth Deformation: Seasonal Cycle Detected

Geoffrey Blewitt, David Lavallée, Peter Clarke and Konstantin Nurutdinov

Science **294** (5550), 2342-2345.
DOI: 10.1126/science.1065328

ARTICLE TOOLS

<http://science.sciencemag.org/content/294/5550/2342>

SUPPLEMENTARY MATERIALS

<http://science.sciencemag.org/content/suppl/2001/12/13/294.5550.2342.DC1>

RELATED CONTENT

<file:/contentpending:yes>

PERMISSIONS

<http://www.sciencemag.org/help/reprints-and-permissions>

Use of this article is subject to the [Terms of Service](#)

Science (print ISSN 0036-8075; online ISSN 1095-9203) is published by the American Association for the Advancement of Science, 1200 New York Avenue NW, Washington, DC 20005. 2017 © The Authors, some rights reserved; exclusive licensee American Association for the Advancement of Science. No claim to original U.S. Government Works. The title *Science* is a registered trademark of AAAS.